www.czasopisma.pan.pl PAN www.journals.pan.pl
POLSKA AKADEMIA NAUK

Arch. Metall. Mater. **70** (2025), 4, 1515-1531

DOI: https://doi.org/10.24425/amm.2025.156232

XIAOLE GE[1,2], I.N. KOLUPAEV[1*], DI JIANG[1,2], SHOUZHEN CAO[2],
WEIWEI SONG[2], HONGFENG WANG[2]

MICROSTRUCTURE AND MECHANICAL PROPERTIES OF Cu-Cu JOINTS FABRICATED BY RFSSW: EFFECT OF PLUNGE DEPTH

Due to the unique physicochemical properties of copper (Cu), conventional fusion welding faces certain challenges when welding this material. In this study, Cu-Cu joints were fabricated using refill friction stir spot welding (RFSSW) at five different plunge depths. The macroscopic morphologies of the welded joints (WJs) under various welding conditions were examined, and the microstructural differences in representative zones of the WJ were analyzed. The microhardness and tensile-shear failure load (T-SFL) of the WJs were evaluated to assess the mechanical performance, and the failure mechanisms were explored. The results indicated that with increasing plunge depth, the microstructure tended to coarsen, accompanied by a gradual decrease in microhardness. The T-SFL initially increased and then decreased with increasing plunge depth, with the optimal depth found to be 1.4 times the plate thickness. For Cu-Cu joints, the softening effect in the heat-affected zone (HAZ) outside the stirring zone is identified as a key factor limiting the load-bearing capacity of the WJs.

Keywords: Cu; RFSSW; Plunge depth; Microstructure; Mechanical properties

1. Introduction

Copper (Cu) is widely used in applications requiring high electrical and thermal conductivity due to its excellent conductive and heat dissipation properties. Such applications include high-power electrical terminals, busbars in new energy vehicle batteries, leads in power inverters, transformer windings, heat exchangers, and radiators [1-4]. In engineering applications, considering factors such as manufacturing, transportation, and installation requirements, Cu is often fabricated into structural components and joined using lap joints. Common methods for joining structural components include mechanical connections and welding. Mechanical connections primarily involve bolted joints and riveting. Bolted joints offer the advantage of easy assembly and disassembly; however, the presence of microscopic gaps between the connecting components increases contact resistance and makes the joint susceptible to loosening [5,6]. While riveting can achieve high connection strength, it also introduces microscopic gaps and is not suitable for use in confined spaces. Given that the melting point of Cu exceeds 1000°C, conventional fusion welding generates a significant amount of harmful gases and spatter [7,8], along with a large heat-affected zone (HAZ) [9], which severely affects weld quality. In the case of brazing, the conductivity of the brazed layer is much lower compared to that of Cu, compromising the electrical performance of the welded joint (WJ) while also making the joint prone to cracking. Additionally, soldering Cu leads to the development of intermetallic compounds in the welded zone, which negatively impacts the electrical and thermal conductivity of the joint. Thus, traditional fusion welding and mechanical joining methods present certain limitations when applied to Cu connections.

Fortunately, the invention of friction stir welding (FSW) has provided a groundbreaking technological solution for achieving high-quality welding of Cu, a material characterized by excellent thermal conductivity and large coefficient of thermal expansion [10-12]. FSW, first introduced by The Welding Institute of UK in 1991, is an advanced solid-state welding process. Its fundamental principle involves generating heat through friction between the tool and the workpiece, bringing the material to a plasticized state. The plasticized material is then stirred and mixed under the mechanical action of the tool, ultimately forming a solid-state joint [13,14]. This welding method offers several advantages, including low welding temperature, minimal deformation, and environmental sustainability. To address the

---

[1] NATIONAL TECHNICAL UNIVERSITY «KHARKIV POLYTECHNIC INSTITUTE», DEPARTMENT OF MATERIALS SCIENCE, KHARKIV, 61002, UKRAINE
[2] HUANGSHAN UNIVERSITY, COLLEGE OF MECHANICAL AND ELECTRICAL ENGINEERING, HUANGSHAN, 245041, P.R. CHINA

* Corresponding author: igor.kolupaev@gmail.com

application demands of localized spot joining, friction stir spot welding (FSSW) was proposed based on the FSW principle [15]. Various types of FSSW have been introduced, including traditional friction stir spot welding (TFSSW) [16,17], swept friction stir spot welding (SFSSW) [18,19], probeless friction stir spot welding (PFSSW) [20,21], and refill friction stir spot welding (RFSSW) [22,23]. Among these, RFSSW has been recognized as one of the most promising alternatives to traditional fusion welding [24]. RFSSW was first proposed by the GKSS Research Center in Germany in 2005 [25]. This welding technique not only eliminates keyhole defects inherent in TFSSW and SFSSW [26], but also addresses the thinning issue in the welding zone associated with PFSSW. By ensuring superior joint integrity, RFSSW has garnered significant research interest in recent years.

In RFSSW, the welding process parameters are critical factors influencing weld quality [27], and have been a focal point of research. Among welding parameters, the tool plunge depth directly affects the size of the welded zone and the material mixing efficiency, thereby impacting the microstructural features and mechanical properties of the WJ [28,29]. Works of literature have demonstrated that plunge depth plays the most crucial role in determining the strength of WJ [30,31]. Notably, the influence of plunge depth on weld quality differs according to the material type and thickness of the workpiece. For example, in the case of 2 mm-thick 6061 aluminum alloy, the tensile-shear failure load (T-SFL) of the WJ first rises and then falls as plunge depth grows, with the optimal plunge depth being equal to the plate thickness [32]. Similarly, for 2 mm-thick 2198 aluminum alloy [33] and 1.9 mm-thick 7B04-T74 aluminum alloy [34], the T-SFL also exhibits an initial increase followed by a decrease as plunge depth increases, with the optimal plunge depths being 1.3 times and 1.6 times the plate thickness, respectively. However, for 3.2 mm-thick 2060 aluminum alloy, within the experimental range, the T-SFL rises with growing plunge depth, with the optimal plunge depth being 1.25 times the plate thickness [35]. Additionally, Zou et al. investigated the welding performance of 2 mm-thick AA2219-O and 8 mm-thick AA2219-C10S aluminum alloys and found that the T-SFL of the WJ continuously decreased with increasing plunge depth, with the ideal plunge depth occurring at 1.1 times the top plate thickness [36]. Yuan et al. explored the influence of plunge depth on the microstructure and mechanical properties of 2 mm-thick Al-Li alloys. Their findings indicated that the T-SFL of the WJ reached its maximum when the plunge depth was 1.25 times the plate thickness [37]. The study conducted by Silva et al. showed that the failure modes of WJs exhibit significant variations under different plunge depths [38]. By examining the microscopic fracture morphologies, such as the shape of dimples, one can gain valuable insights into the underlying failure mechanisms of the joints [39]. Furthermore, from the perspective of the materials to be welded, studies on RFSSW have predominantly concentrated on the welding of aluminum alloys [40-42], magnesium alloys [43-45], and aluminum-copper dissimilar alloys [46-48]. In contrast, relatively limited attention has been given to the welding of Cu, a material with a high melting point and large thermal expansion coefficient. In particular, the impact of plunge depth – an essential parameter – on the microstructure features and mechanical behavior of Cu-Cu joints has not yet been fully revealed. Therefore, further investigation into RFSSW of Cu is necessary.

This work conducted an experimental investigation on RFSSW of Cu, with a particular focus on the impact of plunge depth on joint properties. To achieve this goal, 1 mm-thick Cu plates were used as the welding material, and welding experiments were performed with five different plunge depths. The microstructural evolution of the WJ was analyzed, and the microhardness and T-SFL of the Cu-Cu joints at different plunge depths were evaluated. Additionally, the fracture modes and failure mechanisms were systematically explored.

2. Experimental procedures

2.1. Materials and fabrication

RFSSW achieves material plasticization, stirring, and refilling under thermo-mechanical coupling through the coordinated motion of the clamping ring, sleeve, and probe. The working principle is illustrated in Fig. 1(a). Initially, the clamping ring applies axial pressure downward to secure the workpieces, preventing warping or movement during welding. Simultaneously, the probe and sleeve rotate synchronously at a predetermined speed while contacting the top plate of the workpiece. The frictional heat generated at the contact interface preheats the welding zone. Subsequently, the sleeve plunges downward at a designated speed to a specified depth, while the probe moves upward. The combined effect of the rotational motion and plunging of the sleeve generates frictional heat, softening the material in the welding position. Under the thrust of the sleeve, the softened material migrates toward the upper region, filling the gap left by the probe's ascent. Once the sleeve arrives at the designated position, both the sleeve and probe remain stationary at their lowest and highest positions, respectively, while continuing to rotate. This dwell period ensures sufficient stirring and mixing of the material, a process referred to as the dwell stage I. Following this, the sleeve and probe reverse their motion—the sleeve withdraws vertically as the probe descends, driving the softened material in the void back into the region vacated by the sleeve. When both the sleeve and probe resume their initial positions, the refilling of the cavity is completed, a process known as the refill stage. Subsequently, the sleeve and probe remain at the starting position for another dwell period to ensure uniform material distribution at the surface of the WJ, referred to as the dwell stage II. Finally, the clamping ring, sleeve, and probe move upward simultaneously, marking the completion of the welding process. Generally, the plunge stage and refill stage are indispensable to the welding process, whereas the preheat stage and dwell stages are optional.

The welding experiments were performed using a CNC welding machine manufactured by Beijing FSW Technology

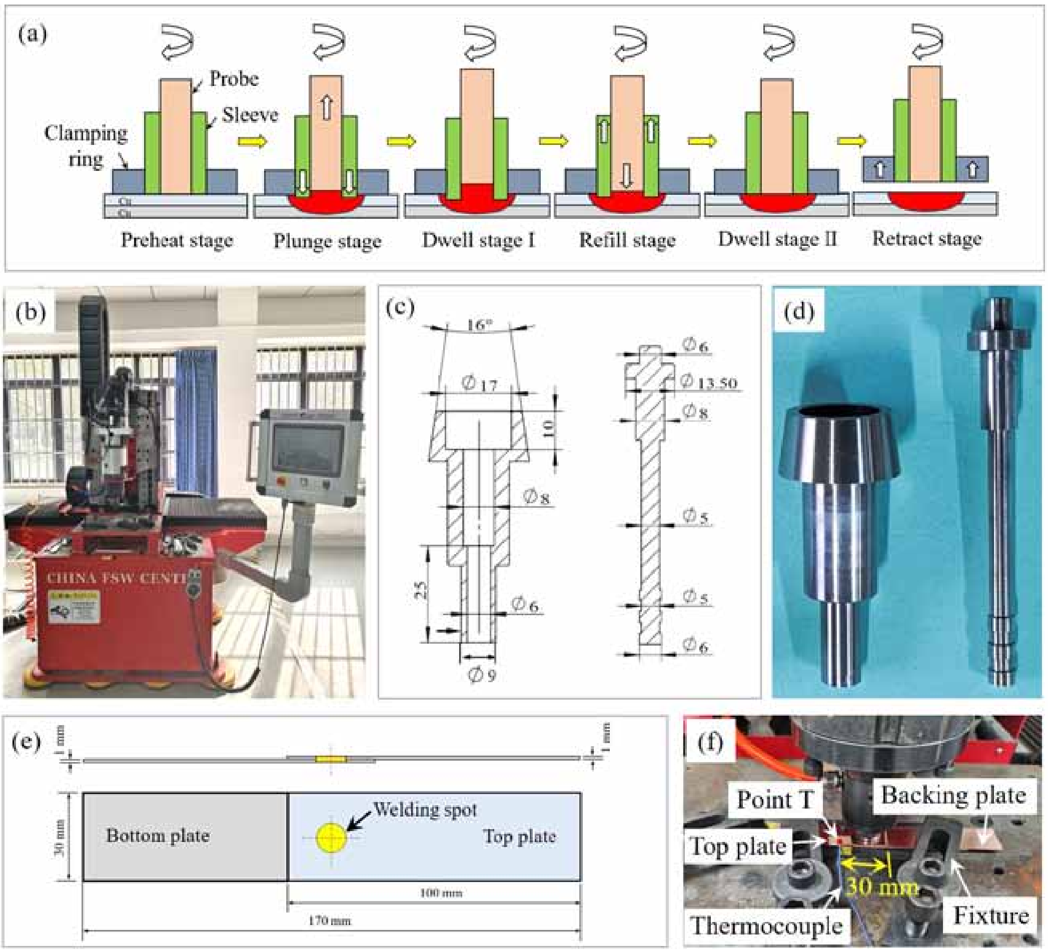

Fig. 1. Welding principles and equipment: (a) Working principle of RFSSW; (b) Welding equipment; (c-d) Sleeve and probe; (e) Dimensions of workpiece; (f) Schematic diagram of welding temperature measurement

Co., Ltd., as shown in Fig. 1(b). A specialized welding tool was designed based on the structural characteristics of the welding machine, with the probe and sleeve diameters measuring 6 mm and 9 mm, respectively, as illustrated in Figs. 1(c-d). The tool was made of SKH-9 high-speed steel. The workpieces used in this study were T2 Cu plates, with dimensions of 100×30×1 mm, supplied by Dongguan Shengxiang Metal Materials Co., Ltd. TABLE 1 presents the chemical composition of the T2 Cu plates. The welding process was conducted in accordance with the National Standard of the People's Republic of China, GB/T 41979.5-2022 [49]. During welding, the top and bottom plates were positioned in an overlapping configuration with a lap size of 30×30 mm, as shown in Fig. 1(e). To systematically analyze the influence of plunge depth on the microstructure and mechanical properties of WJs, and to explore the widest possible lower and upper limits of the parameter range, five plunge depths of 0.6 mm, 0.8 mm, 1.0 mm, 1.4 mm, and 1.6 mm were selected for welding experiments, corresponding to conditions where the plunge depth was less than, equal to, and greater than the plate thickness. The other process parameters were kept constant, including the clamping force (7 kN), tool rotational speed (1200 rpm), plunge speed (30 mm/min), preheating time (3 s), dwell time I (2 s), and dwell time II (3 s). The welding temperature was measured using a thermocouple placed at the boundary on the surface of the top plate, 30 mm from the right edge of the top plate, as shown in Fig. 1(f). A temperature data logger was used to record the measured temperatures, with a sampling frequency of one measurement per second.

2.2. Tests and characterization

For cross-sectional macrostructure and microstructure observations, the welded workpieces with different plunge depths were sectioned through the weld center using a wire cutting machine. The cutting position and size of the welded workpieces are shown

TABLE 1

Chemical composition of T2 Cu plate

Element	Cu+Ag	Bi	Sb	As	Fe	Pb	S	Residuals
Weight (wt.%)	99.90	0.001	0.002	0.002	0.005	0.005	0.005	0.08

in Fig. 2(a). The observation surfaces were polished using silicon carbide sandpaper until no visible scratches remained. Subsequently, the surfaces were electropolished to remove residual scratches. The electropolishing solution consisted of nitric acid and methanol (HNO_3: CH_3OH = 20 ml: 80 ml), with the process carried out at 30 V, 1 A, and for 12 s. After electropolishing, the polished surfaces were chemically etched using a metallographic etchant and then examined under an optical microscope for microstructure observation. The etchant composition consisted of ferric chloride, hydrochloric acid, and water ($FeCl_3$: HCL: H_2O = 5 g: 15 ml: 100 ml). For Electron Backscatter Diffraction (EBSD) analysis, the sample preparation followed the same procedure as metallographic testing. EBSD measurements were carried out using a Hitachi scanning electron microscope (SEM) fitted with an Oxford Instruments probing system.

For the microhardness tests on both the cross-section and surface, the workpieces were first sectioned using a wire cutting machine, as shown in Fig. 2(a). The test surfaces were then ground and polished using silicon carbide sandpaper and a polishing machine. Microhardness measurements of the WJs were conducted using a microhardness tester with an applied force of 300 g and a holding time of 10 s. The positions and distributions of the microhardness test points on the cross-section and surface are shown in Figs. 2(b-d). The T-SFL of the lap joints was tested using a universal tensile testing machine at a tensile speed of 1.5 mm/min. Two tensile tests were conducted for each plunge depth, and the arithmetic mean of the results was taken as the final tensile test value.

3. Results

3.1. Macroscopic characteristics

Fig. 3 shows the surface morphology of the WJs at different plunge depths. As observed in Figs. 3(a-b), the WJs exhibit relatively smooth surfaces across all plunge depths. Distinct heat input traces are visible on the joint surfaces, and the width of heat input increases from 29 mm to 44 mm as the plunge depth increases. Furthermore, distinct demarcations are visible between the probe stirring zone (PSZ) and the sleeve stirring zone (SSZ), and between the SSZ and the unprocessed region.

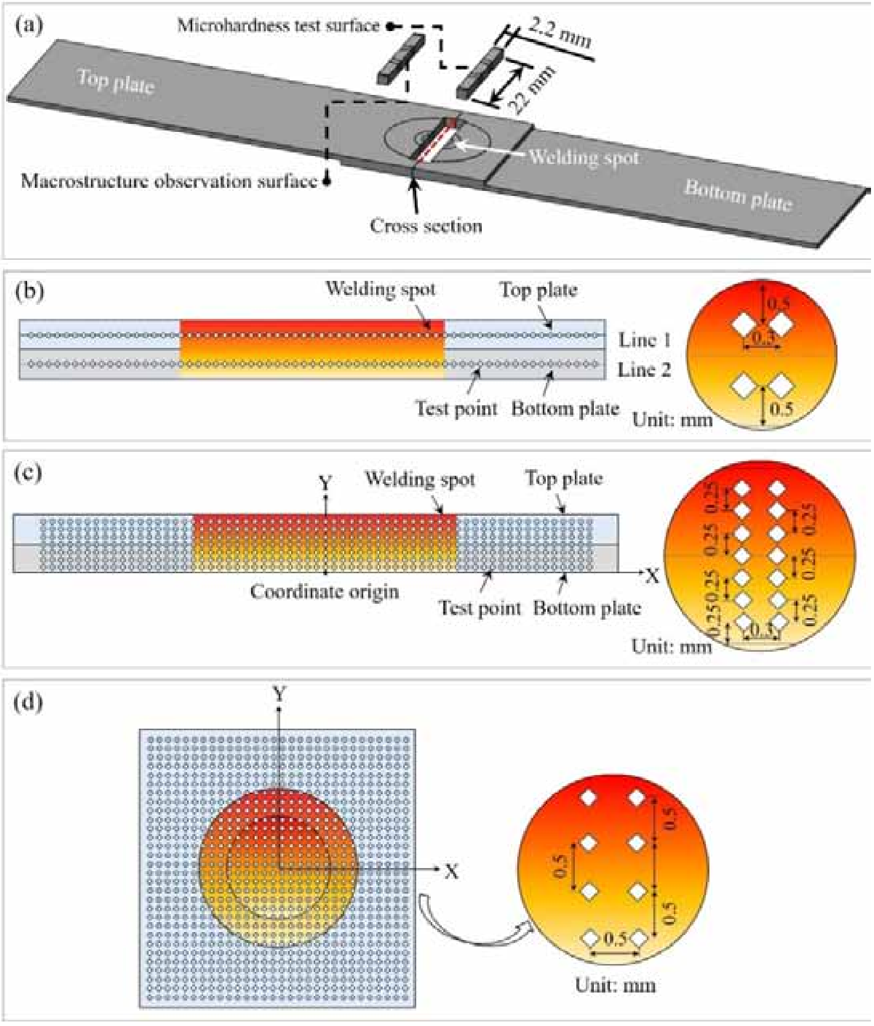

Fig. 2. Schematic diagram of workpiece cutting and distribution of microhardness test points: (a) Cutting positions of metallographic observation specimen and microhardness test specimen; (b) Cross-sectional microhardness curve test; (c) Cross-sectional microhardness cloud map test; (d) Surface microhardness cloud map test

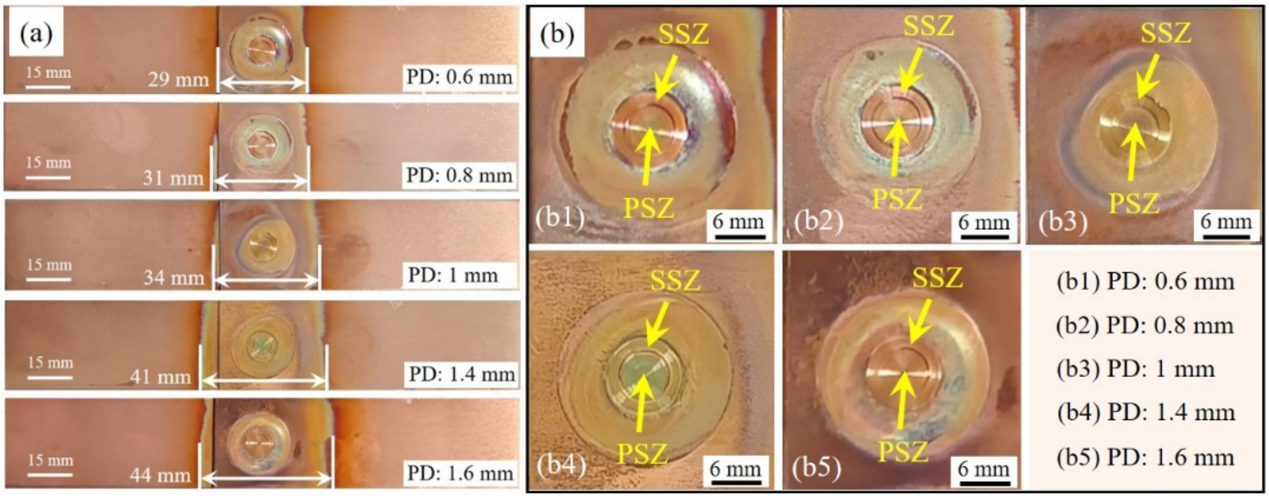

Fig. 3. Appearance of WJs: (a) Images of welding workpieces; (b) Enlarged views of welding spots under different plunge depth

Fig. 4 presents the cross-sectional features of the WJs at different plunge depths. It can be observed that the cross-sectional morphology exhibits an approximately symmetrical structure. Based on the microstructural variations across different zones, the WJ can be classified into three distinct zones: the stirring zone (SZ), the thermo-mechanically affected zone (TMAZ), and the heat-affected zone (HAZ). The SZ consists of both the PSZ and the SSZ. As the plunge depth increases, the stirring range of the tool expands, the stirring duration prolongs, and the extents of both the SZ and the TMAZ continue to enlarge. To clearly reveal the interface characteristics between the top and bottom plates, the cross-sections in Fig. 4 were not subjected to metallographic etching. Therefore, no obvious differences can be observed among the SZ, TMAZ, and HAZ at different plunge depths in Fig. 4.

A W-shaped bonding ligament is seen between the top and bottom plates. As the plunge depth increases, the material flowability and mixing effect in the welded zone improve, leading to an expansion of the bonding ligament toward both ends of the WJ. The bonding ligament refers to a ligament-like structure formed

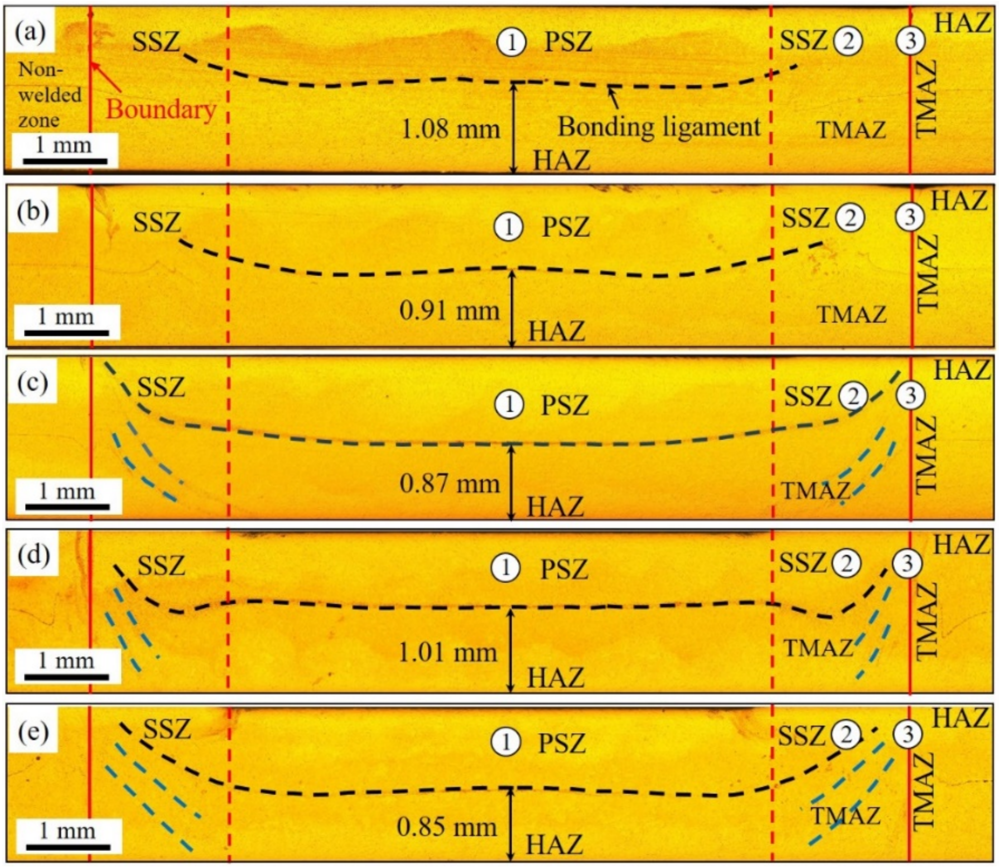

Fig. 4. Cross-sectional features of WJs at different plunge depths: (a) 0.6 mm; (b) 0.8 mm; (c) 1 mm; (d) 1.4 mm; (e) 1.6 mm

between the top and bottom plates under the stirring action of the tool during welding. Its formation is closely related to material plastic flow and welding parameters, and its morphological characteristics influence the bonding quality between the top and bottom plates. Unlike the well-defined and relatively wide bonding ligaments commonly observed in aluminum and magnesium alloys [50-52], only a fine ligament line was observed in Cu-Cu joints. This phenomenon may be ascribed to the excellent plasticity, toughness, and thermal conductivity of Cu, which enable better adaptation to material flow and deformation during welding. The efficient heat dissipation in Cu further promotes enhanced bonding between the top and bottom plates, resulting in a finer and more uniform bonding ligament.

Fig. 5 shows the Hook morphology in the cross-section at different plunge depths. The formation of Hook is closely associated with welding parameters and is generally considered to introduce discontinuities or weak zones at the interface between the top and bottom plates, which are highly susceptible to crack initiation or stress concentration [22,29,53]. It is observed that when the plunge depth is below the thickness of the top plate (1 mm), only slight downward bending occurred at the interface outside the SZ. This is primarily because, at small plunge depths, the tool does not fully penetrate the top plate, and the welding temperature remains relatively low, limiting material flow within the WJ. Consequently, no pronounced Hook feature, typically caused by intense material flow, is formed. When the plunge depth is 1 mm, the bending extent of the Hook increases, and its height reaches 0.22 mm. At a plunge depth of 1.4 mm, the Hook initially bends downward and then upward. When the plunge depth further rises to 1.6 mm, the Hook first bends upward by 0.52 mm and then curves downward. Overall, for plunge depths of 1 mm and below, the Hook primarily exhibits a downward bending morphology, whereas at plunge depths of 1.4 mm and 1.6 mm, the Hook exhibits an upward bending morphology. The Hook height tends to rise with the increase of the plunge depth. This variation is attributed to the intensified stirring of the material in the SZ at large plunge depths, which significantly enhances material flowability. As a result, the material in the SZ undergoes extensive plasticization, with a greater volume of material being pushed toward the periphery of the SZ. During this process, the material flow direction shifts from downward to outward, gradually overflowing beyond the SZ. Additionally, during the refilling process, the retraction of the sleeve further drives the already softened material outside the SZ to flow upward, exacerbating the upward bending of the Hook.

3.2. Welding temperature

Fig. 6 shows the temperature variation curves at point T (see Fig. 1(f)) under different plunge depths. It can be observed that the welding temperature gradually increases after the start of welding, reaches a peak just before the end of welding, and then gradually decreases to room temperature. With the increase in

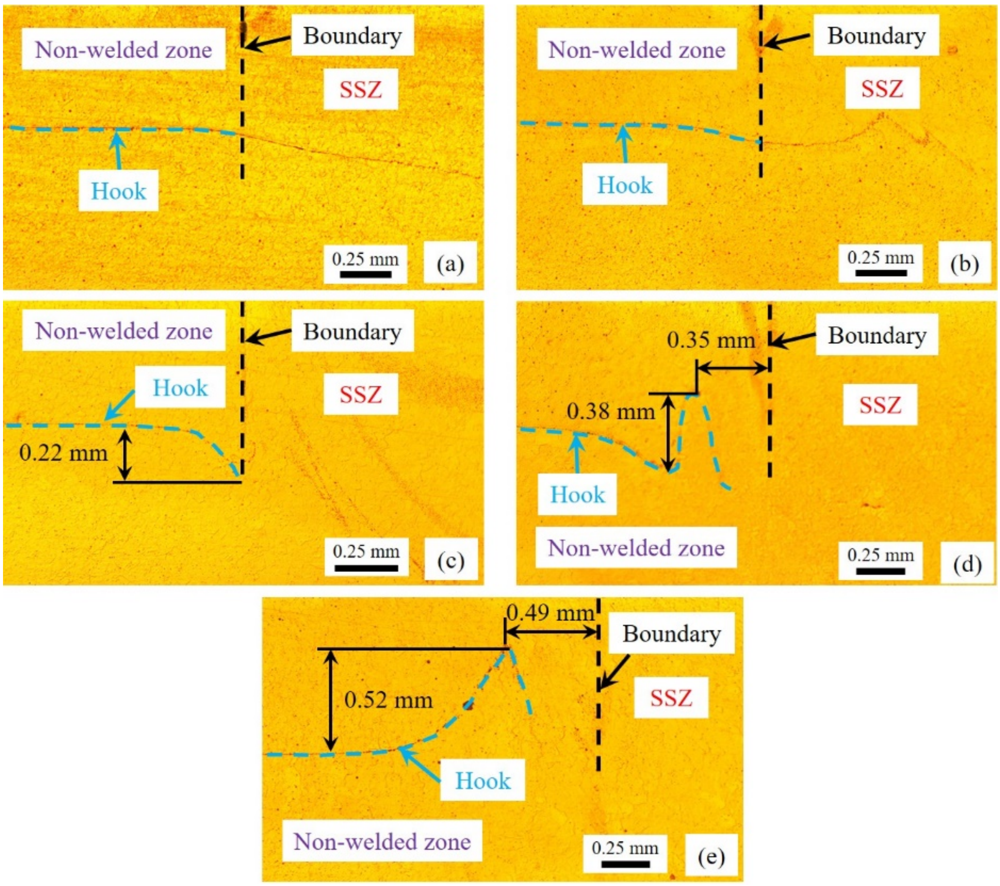

Fig. 5. Cross-sectional Hook morphology at different plunge depths: (a) 0.6 mm; (b) 0.8 mm; (c) 1 mm; (d) 1.4 mm; (e) 1.6 mm

plunge depth, the peak temperature of welding continues to rise. When the plunge depth reaches 1.6 mm, the peak temperature is 2.25 times that at 0.6 mm. This rise in welding temperature is mainly attributed to the increased contact area between the tool and the material, as well as the prolonged welding time at greater plunge depths. Therefore, it can be concluded that the greater the plunge depth, the higher the peak temperature during welding and the greater the heat input.

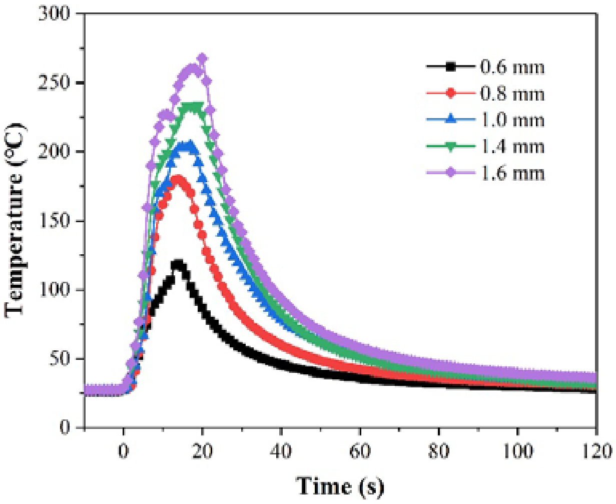

Fig. 6. Temperature variation curves under different plunge depths

3.3. Microstructural features

Fig. 7 presents the microstructure of the PSZ (Position ① in Fig. 4) at different plunge depths. It can be observed that as the plunge depth rises, the microstructure within the SZ shows a tendency for coarsening, mainly due to the prolonged welding time associated with greater plunge depths. When the plunge depth rises from 0.6 mm to 1.6 mm, the total welding time extends by a factor of 1.38. The extended welding time grows the heat input during the welding process, leading to a rise in welding temperature. The relationship between temperature and grain growth rate can be expressed as [54]:

$$\frac{d\bar{D}}{dt} = K_1 \frac{1}{\bar{D}} e^{-Q_m/(RT)} \tag{1}$$

where, $d\bar{D}/dt$ is the growth rate of the average grain diameter, K_1 is a constant, Q_m is the activation energy of grain boundary migration, R is the average grain radius, and T is the temperature. Evidently, higher temperatures result in a faster grain growth rate. Therefore, the increase in welding time raises the welding temperature, which in turn accelerates grain coarsening.

Fig. 8 shows the EBSD results for different positions at a plunge depth of 1.4 mm. It can be seen that the grain size in the parent material is relatively small, with grain diameters predominantly ranging from 2 to 8 μm and an average grain diameter of only 3.28 μm. Compared to the parent material, the grain size within the welded zone rises significantly. Notably, the average grain size in the PSZ is the largest, reaching 19.65 μm – approximately six times that of the parent material. The grain size distribution in the SZ is influenced by both the welding temperature and the tool mechanical stirring effect. It is evident that in the welding of Cu, welding temperature plays a dominant role in grain coarsening. It is worth noting that, compared to the SSZ and the HAZ, grains at the boundary of the SZ undergo significant refinement. The grain refinement in this zone is strongly influenced by the thermo-mechanical interaction the material undergoes. Firstly, although the peak temperature during the welding process is primarily concentrated in the PSZ [55,56], the high thermal conductivity of Cu results in significant heat transfer to the boundary zone. Consequently, the material at the boundary is still subjected to considerable thermal input, and the sustained high-temperature environment facilitates the occurrence of dynamic recrystallization. Secondly, the material at the boundary experiences the highest stress and strain due to the stirring action of the sleeve [31,57], leading to severe strain accumulation in this zone, which promotes grain fragmentation near the boundary. Therefore, the boundary of

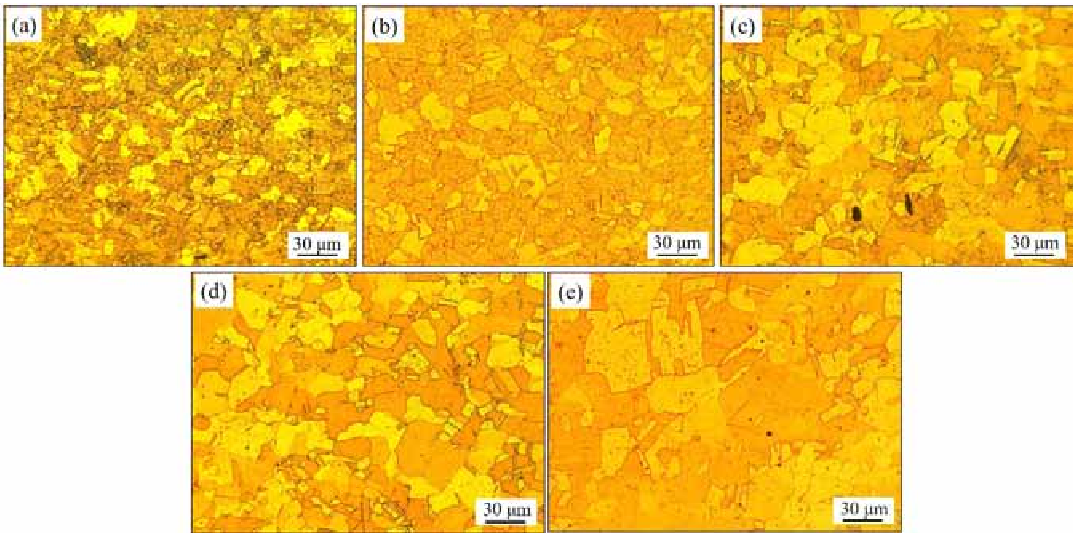

Fig. 7. Microstructure of the PSZ at different plunge depths: (a) 0.6 mm; (b) 0.8 mm; (c) 1 mm; (d) 1.4 mm; (e) 1.6 mm

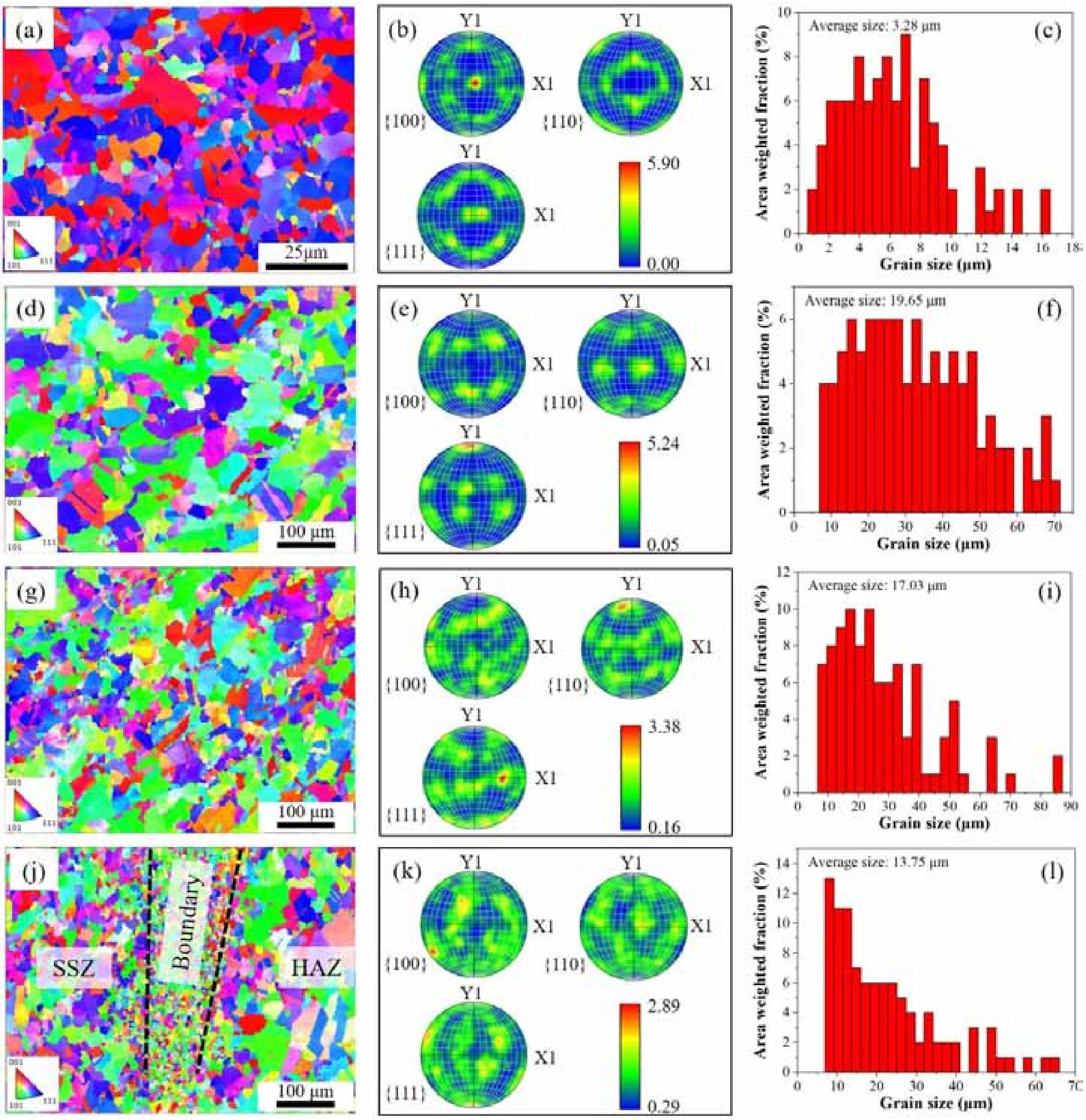

Fig. 8. IPF map, pole map and grain size distribution diagram of different positions: (a-c) Parent material; (d-f) Position ① in the PSZ; (g-i) Position ② in the SSZ; (j-l) Position ③ at the boundary

the SZ is characterized by the superposition of intense thermal and strain gradients. In this zone, not only is the temperature elevated, but the material is also subjected to complex stress and strain state, which promotes the refinement of grains. From the pole map, a strong rolling orientation is present in the parent material, with a maximum pole density of 5.90. The maximum pole density in the welded zone is lower than that of the parent material, and with increasing distance from the weld center, the maximum pole density progressively diminishes, indicating a weakening of the orientation.

Fig. 9 presents the Kernel Average Misorientation (KAM) maps and the DefRex maps for different zones at a plunge depth of 1.4 mm. The KAM maps reflect the distribution of local strain and dislocations in the material. As shown in Figs. 9(a-d), the KAM in the SZ are more pronounced compared to the parent material, with the SSZ exhibiting the most prominent KAM. This phenomenon is attributed to the intense thermo-mechanical coupling effect in this zone, leading to greater plastic deformation and higher dislocation density. Figs. 9(i) and (m) reveal that sub-grains are predominant in the parent material, with only a small proportion of deformed grains. In the PSZ, sub-grains remain predominant; however, due to the tool stirring effect, the proportion of deformed grains increases, as shown in Figs. 9(j) and (n). Notably, the SSZ shows the largest share of deformed grains, reaching 58% (see Figs. 9(k) and (o)), which is a result of the intense plastic deformation in this zone. As shown in Figs. 9 (l) and (p), the proportion of recrystallized grains increases significantly near the boundary of the SZ, with recrystallized grains primarily distributed at the boundary. This observation suggests that the material in this zone undergoes extensive recrystallization under the combined effects of mechanical stirring imposed by the sleeve and high temperature. This recrystallization process is a key factor in the development of fine grains in this region.

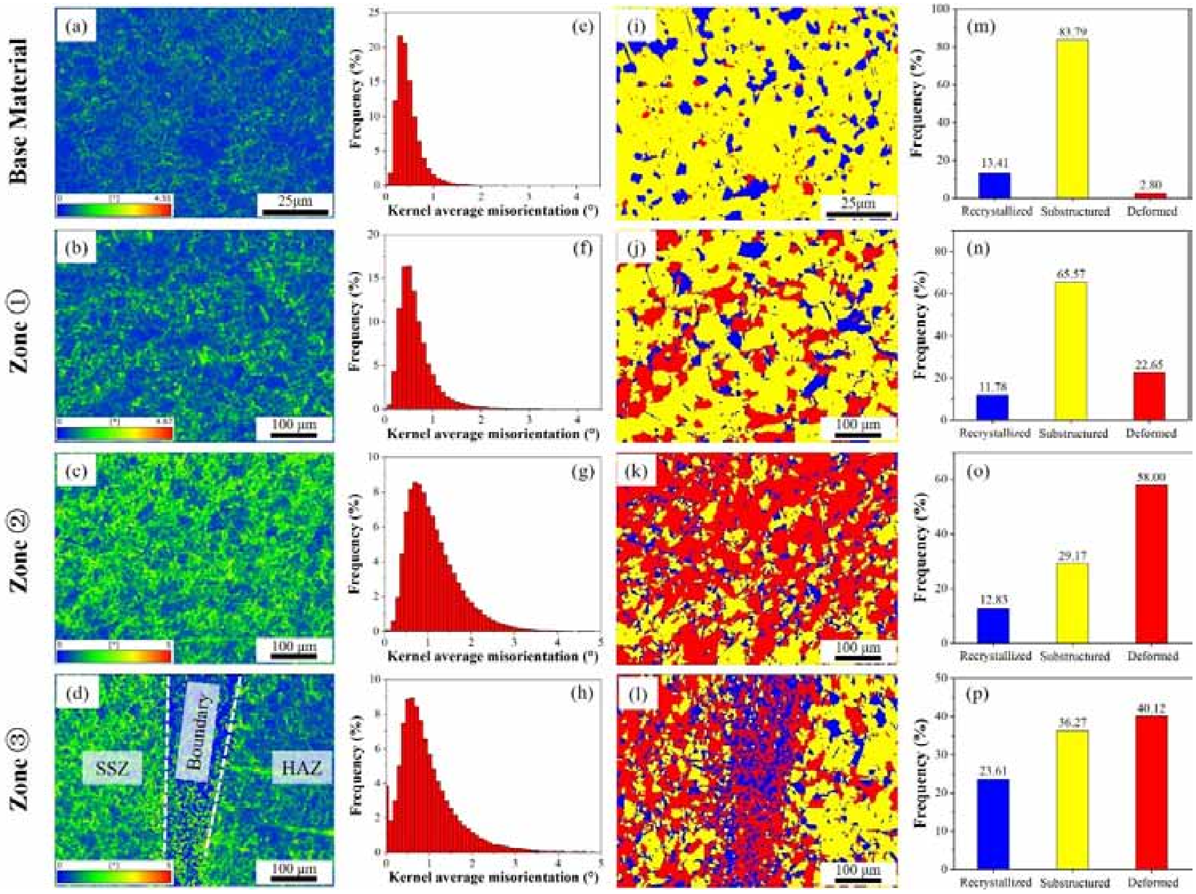

Fig. 9. KAM and DefRex maps of different positions: (a-d) KAM maps; (e-h) Misorientation distribution diagrams; (i-l) DefRex maps; (m-p) Volume fractions of different types of grains

3.4. Microhardness profile

Fig. 10 presents the microhardness distribution at different plunge depths. As shown in Figs. 10(a-e), the microhardness profiles exhibit a similar trend across different plunge depths. The microhardness of the parent material is approximately 90 HV. As the measurement points move from the parent material toward the welded zone, the microhardness gradually decreases, reaching a minimum near the outer region of the SZ. This outer region corresponds to the HAZ, which is primarily influenced by the high temperatures during welding, leading to coarsening of the microstructure. According to the Hall-Petch equation [58,59]:

$$\sigma_s = \sigma_0 + \frac{k_y}{\sqrt{d}} \tag{2}$$

where, σ_s is the yield strength (MPa), σ_0 is a value related to the crystal type, k is a constant, and d is the grain diameter. It follows that larger grain sizes result in lower yield strength. The relationship between microhardness and yield strength can be expressed as [60]:

$$\sigma_s = \frac{H}{C} \tag{3}$$

where, H represents Vickers hardness (HV) and C is a material-dependent constant (HV/MPa). The correlation between microhardness and grain size is given by:

$$H = C\left(\sigma_0 + \frac{k_y}{\sqrt{d}}\right) \tag{4}$$

Therefore, the larger grain sizes correspond to lower microhardness, which explains the rapid decrease in microhardness within the HAZ.

As the measurement points move from the HAZ toward the SSZ, the microhardness increases. Microstructural analysis indicates that the grains in the SSZ are relatively fine, and this grain refinement is the primary factor contributing to the higher microhardness in this zone. However, as the measurement points progress from the SSZ toward the PSZ, the microhardness exhibits a declining trend, reaching its minimum at the center of the PSZ. This phenomenon results from the limited mechanical stirring effect exerted by the sleeve and the probe at the center of the PSZ. Instead, the high temperatures during welding predominantly influence the microstructural evolution in this zone, promoting grain growth and consequently leading to lower microhardness values.

It should be noted that when the plunge depth is 0.6 mm, the microhardness values at both ends of the curve are close to those of the parent material. This indicates that under this welding

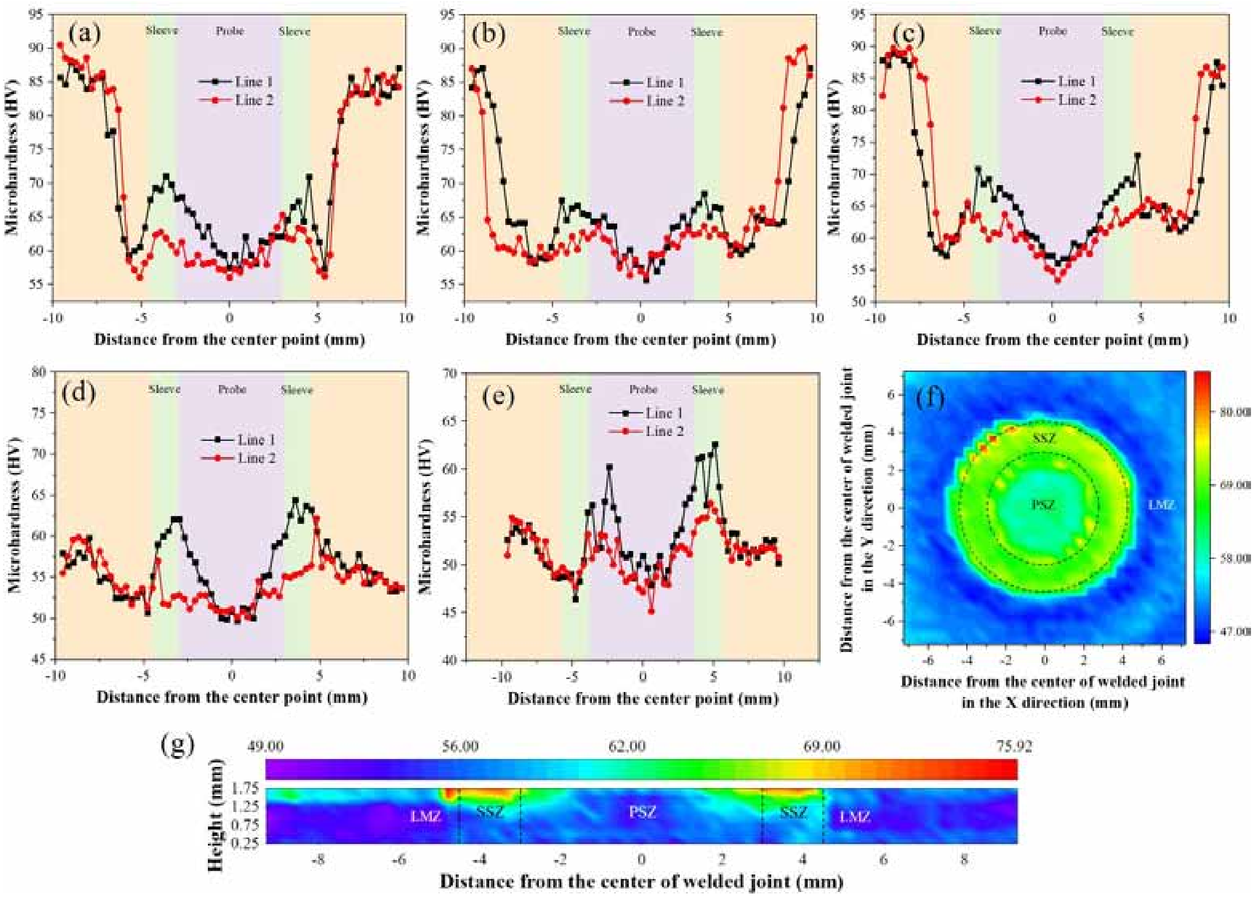

Fig. 10. Microhardness at different plunge depths: (a) 0.6 mm; (b) 0.8 mm; (c) 1 mm; (d) 1.4 mm; (e) 1.6 mm; (f) Surface microhardness cloud map under a plunge depth of 1.4 mm; (g) Cross-sectional microhardness map under a plunge depth of 1.4 mm

condition, the heat input is limited, resulting in a relatively small HAZ outside the SZ. As the plunge depth increases, the heat input during welding rises, leading to an expansion of the HAZ. Consequently, the microhardness values at both ends of the curve tend to decrease, and the minimum microhardness within the SZ also progressively declines. When the plunge depth reaches 1.4 mm, the influence range of the HAZ is significantly enlarged, with the microhardness at both ends of the curve declining to 55 HV and the microhardness at the center of the PSZ decreasing to 50 HV. At a plunge depth of 1.6 mm, the microhardness at both ends further declines to 51 HV, while the microhardness at the center of the PSZ reaches 45 HV, which is only 50% of the parent material. This suggests that an excessively large plunge depth severely weakens the microhardness of the WJ.

As shown in Figs. 10(f-g), the largest microhardness in the welded zone is observed at the upper region of the SSZ, reaching a maximum of 76 HV, which corresponds to 84% of the parent material. Along the height direction of the SSZ, the microhardness gradually decreases from top to bottom. This phenomenon arises from the refilling of material at the top of the SSZ in the final stage of welding, where it remains under sustained mechanical stirring by the sleeve and probe until welding concludes, contributing to finer microstructures in this zone. It is important to note that a lower-microhardness zone (LMZ) forms in the HAZ outside the SSZ owing to the influence of larger heat input. The microhardness in this LMZ is lower than that in both the SSZ and the PSZ, which could negatively affect the strength of the welded workpiece.

3.5. Tensile-shear failure load

Fig. 11 illustrates the tensile-shear performance of the WJs at different plunge depths. It is evident that as the plunge depth increases, the T-SFL first rises and then decreases. The maximum T-SFL is achieved at a plunge depth of 1.4 mm, reaching 5267 N. At smaller plunge depths (0.6 mm and 0.8 mm), the mechanical stirring effect of the tool is relatively weak, and the heat input is low, resulting in limited bonding between materials within the WJ. When the tool penetrates the top plate, it directly facilitates sufficient stirring and mixing of materials between the top and bottom plates, thereby improving the bonding quality of the WJ. However, when the plunge depth further rises to 1.6 mm, the T-SFL decreases to 4788 N. This decline may be attributed to the excessively high welding temperature at this plunge depth, which leads to severe grain coarsening in the microstructure near the WJ. These findings suggest that when the top and bottom plates have the same thickness, a plunge depth of 1.4 times the single-plate thickness enables the Cu welded workpiece to achieve a higher load-bearing capacity.

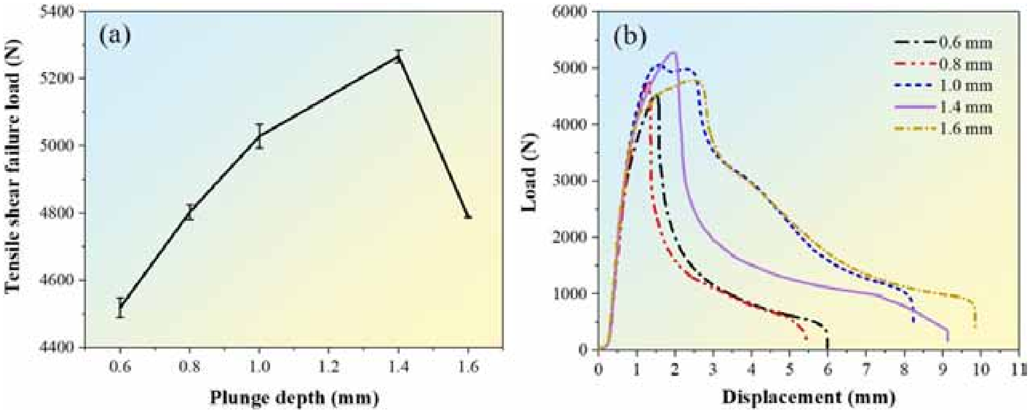

Fig. 11. Tensile-shear performance at different plunge depths: (a) T-SFLs; (b) Displacement-load curves

3.6. Failure mechanism

In RFSSW, common failure modes of welded workpieces include shear-type failure, plug-type failure, and shear-plug mixed failure [61-63]. The failure mode primarily depends on the material bonding quality and the stress distribution in different regions of the WJ. Fig. 12 presents the failure modes of WJs at different plunge depths. As shown in Fig. 12(a), the top plate completely detaches from the WJ, with the joint remaining in the bottom plate, which is characteristic of plug-type failure [64,65]. In contrast, another fracture mode, depicted in Fig. 12(b), occurs when the top plate fractures at the outside of

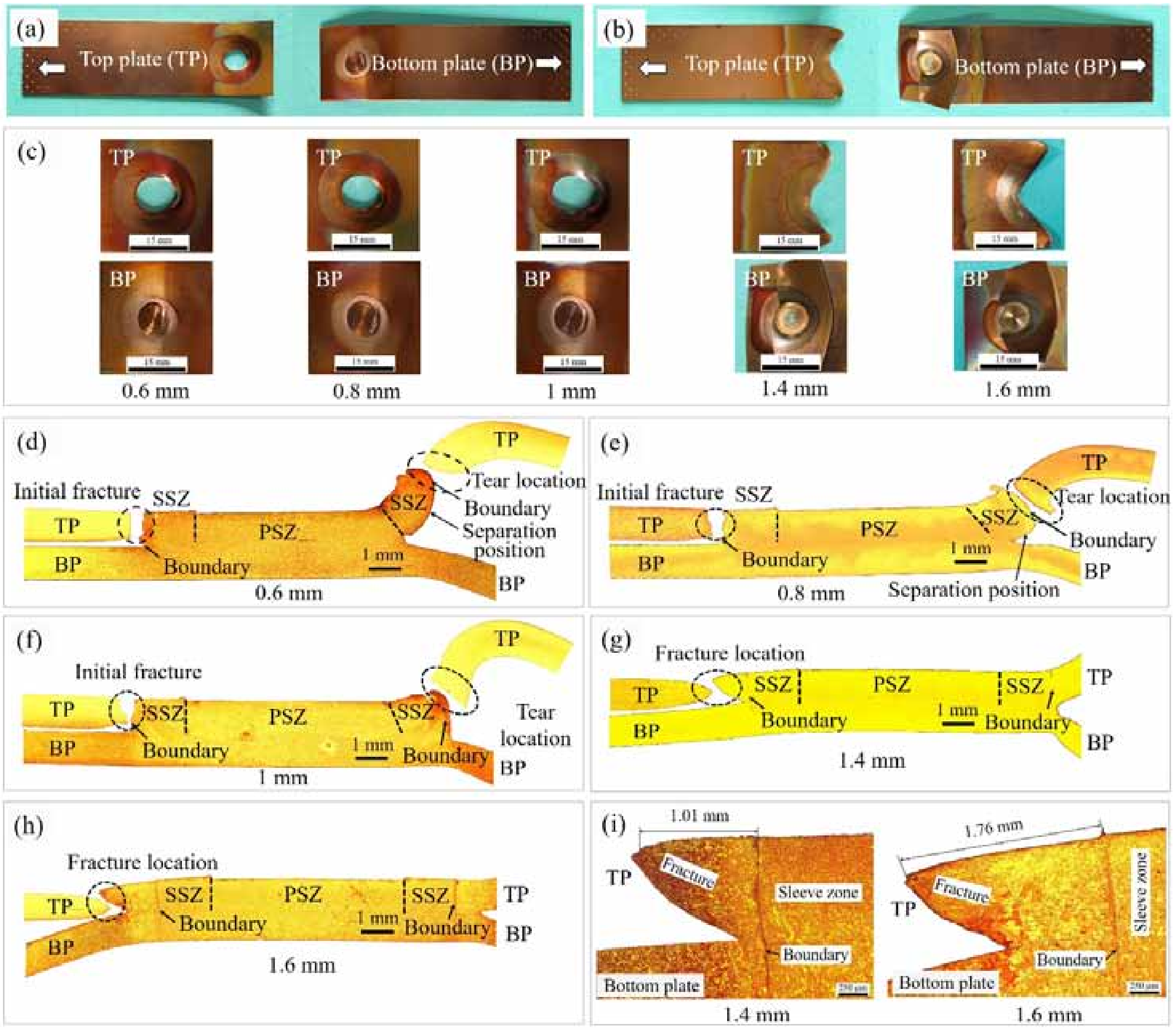

Fig. 12. Failure modes of welding workpieces under different plunge depths: (a) Failure mode under 0.8 mm plunge depth; (b) Failure mode under 1.4 mm plunge depth; (c) Fracture images of welding workpieces under different plunge depths; (d-h) Cross-sectional morphologies of the fractured workpieces under different plunge depths; (i) Enlarged views of the fracture location under plunge depths of 1.4 mm and 1.6 mm

the SZ, with its tensioned end completely separating from the workpiece while the SZ and the free end of the top plate remain bonded to the bottom plate. In this study, this mode of fracture is defined as top-plate-type failure, which has also been observed in aluminum alloy WJ [41]. As illustrated in Fig. 12(c), plug-type failure is the predominant failure mode in workpieces welded with plunge depths ranging from 0.6 mm to 1.0 mm, whereas top-plate-type failure occurs at plunge depths of 1.4 mm and 1.6 mm. Figs. 12(d-f) show that in plug-type failure, the failure location is consistently at the outer edge of the SSZ. At plunge depths of 0.6 mm and 0.8 mm, separation arises between the underside of the SSZ in the top plate and the top surface of the bottom plate. This is due to the insufficient penetration of the tool into the bottom plate, resulting in inadequate material mixing between the top and bottom plates solely by mechanical stirring at the sleeve bottom. Consequently, the bonding effectiveness between the top and bottom plates is compromised. In contrast, in top-plate-type failure, the failure location is always at the outside of the WJ, with no fractures occurring within the SSZ or PSZ, as shown in Figs. 12(g-i). At a plunge depth of 1.4 mm, the fracture position is 1.01 mm from the boundary of the SSZ. As the plunge depth increases, this distance also increases, reaching 1.76 mm at a plunge depth of 1.6 mm.

To understand the stress distribution in welded workpieces under tensile loading, finite element analysis was conducted using Ansys Workbench. For simplification, the following assumptions were made: (i) the material of the welded workpiece was considered homogeneous, and variations in material properties within the WJ were not taken into account; (ii) the contact area between the top and bottom plates was modeled as a 9 mm circular region to simulate the WJ's bonding effect; (iii) the influence of residual stress within the WJ was neglected [66]. The end face of the top plate was fixed, while a displacement boundary condition of 1 mm was applied to the bottom plate. The simulation results are shown in Fig. 13. It can be observed that during tensile loading, stress and strain are primarily concentrated at two locations: the junction between the bottom region of the top plate and the SZ (Zone A) and the junction between the top region of the bottom plate and the SZ (Zone B). Moreover, the stress type in both regions is tensile stress [67], indicating that these two regions are most susceptible to internal crack formation under tensile loading [68,69].

To identify the initiation sites of different failure modes, the SEM was used to capture the morphology of the original crack surfaces, as shown in Fig. 14. Figs. 14(a-c) indicate that at a plunge depth of 0.6 mm, the original crack occurs at the bottom of the tool's maximum plunge depth and propagates along the boundary of the SSZ. Small dimples can be observed in the original crack surface, but their quantity is limited. At a plunge depth of 0.8 mm, the original crack also originates at the maximum plunge depth of the sleeve and extends along the boundary of the SSZ, where dimples and significant plastic deformation are observed, as shown in Figs. 14(d-f). At a plunge depth of 1.0 mm, the original crack occurs near the bottom region of the top plate and propagates along the boundary of the SSZ, with visible dimples and tearing ridges in the original crack surface,

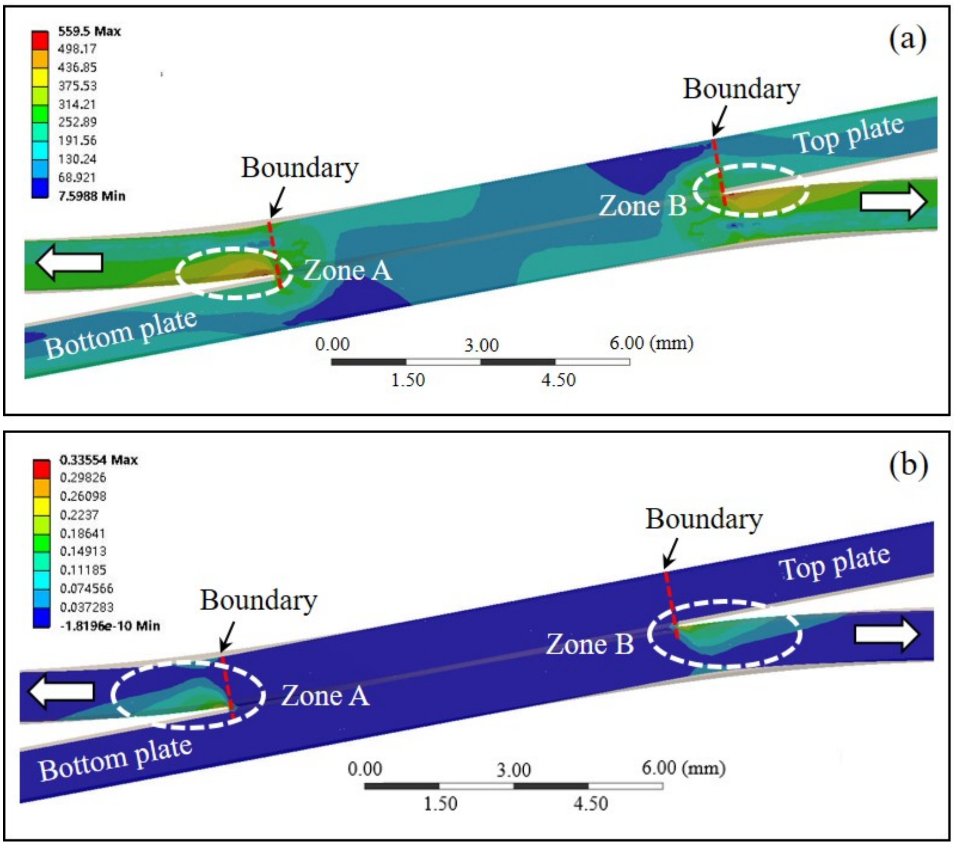

Fig. 13. Finite element simulation results: (a) Von-Mises stress cloud map at the cross section; (b) Strain cloud map at the cross section

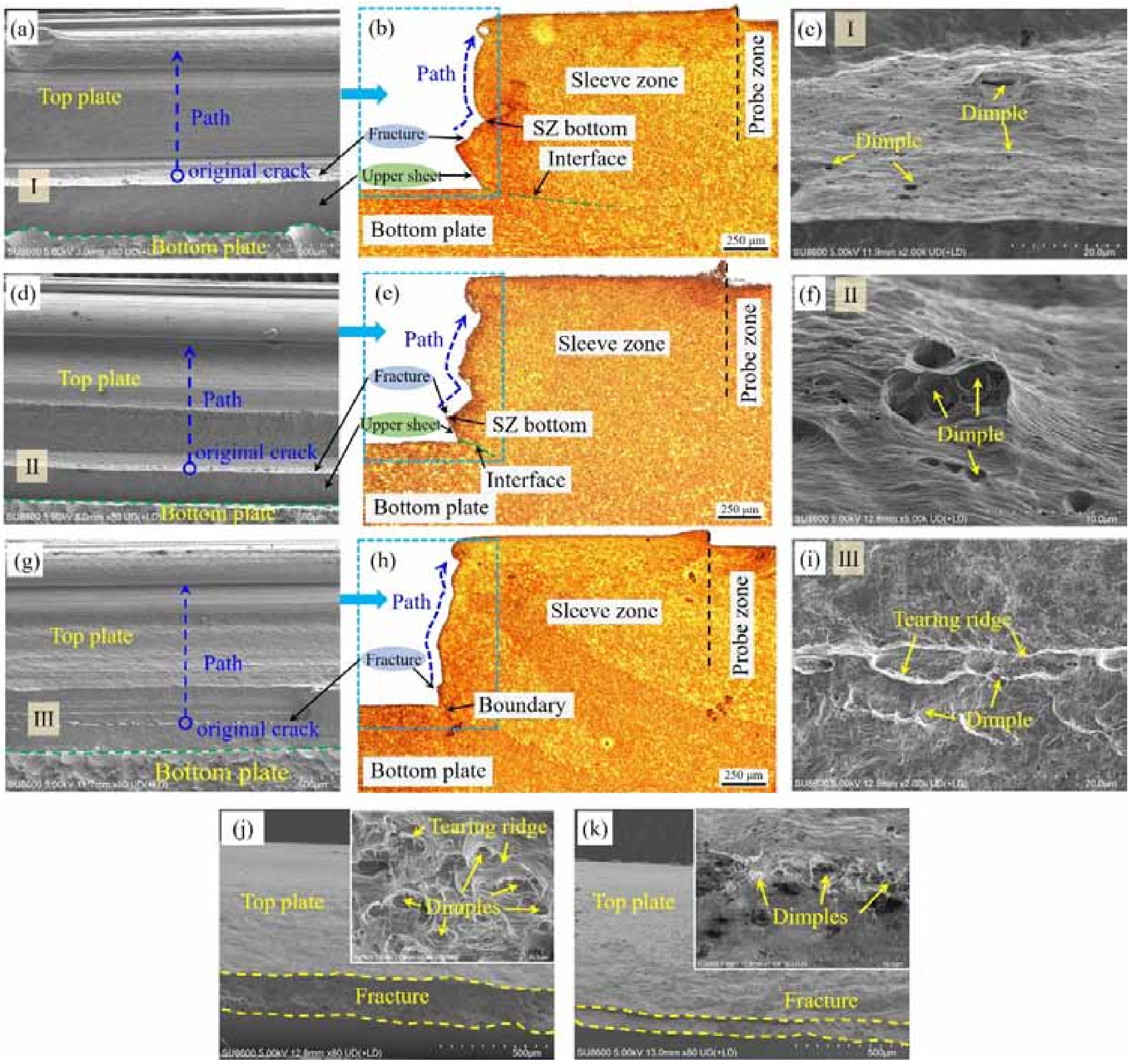

Fig. 14. Fracture morphologies under different failure modes: (a-c) Fracture morphologies under 0.6 mm plunge depth, (a) SEM map under 0.6 mm plunge depth, (b) Coss-sectional morphology under 0.6 mm plunge depth, (c) SEM map at position I; (d-f) Fracture morphologies under 0.8 mm plunge depth, (d) SEM map under 0.8 mm plunge depth, (e) Cross-sectional morphology under 0.8 mm plunge depth, (f) SEM map at position II; (g-i) Fracture morphologies under 1 mm plunge depth, (g) SEM map under 1 mm plunge depth, (h) Cross-sectional morphology under 1 mm plunge depth, (i) SEM map at position III; (j) Fracture morphologies under 1.4 mm plunge depth; (k) Fracture morphologies under 1.6 mm plunge depth

as shown in Figs. 14(g-i). These findings indicate that for plug-type failures, the original crack consistently stems from near the bottom region of the tool's maximum plunge depth. This phenomenon can be attributed to several factors. Firstly, when the plunge depth does not exceed the thickness of the top plate, the limited heat input and material plastic flow capacity result in poor bonding at the bottom of the maximum plunge depth, thereby facilitating the formation of original cracks. Secondly, as shown in Fig. 13, the highest stress and strain under tensile loading occur at the bottom of the tensioned top plate, where the stress type is tensile stress. This promotes significant plastic deformation at the bottom of the top plate, serving as the driving force for the initiation of fractures in this region.

As shown in Figs. 14(j-k), in top-plate-type failure, the original crack occurs at the bottom region of the top plate, primarily due to the significant stress experienced by this region during tensile loading. The original crack surfaces exhibit distinct dimple features, with a greater number and larger size of dimples compared to plug-type failures. This indicates that workpieces undergoing top-plate-type failure experience greater tensile loading and plastic deformation prior to failure, which is consistent with the variation in the T-SFL of the welded workpieces. The dimples observed on the fracture surface exhibit a circular morphology. According to the classification in [39], these dimples are identified as separation dimples, indicating that the failure mode of the WJ is ductile fracture. As depicted in Fig. 12, in top-plate-type failures, the fracture occurs within a range of 1.01 mm to 1.76 mm away from the SZ boundary. This phenomenon results from a variety of factors. Firstly, at plunge depths of 1.4 mm to 1.6 mm, the tool penetrates into the bottom plate, and the increased heat input enhances material flowability, leading to improved mixing between the top and bottom plates in the WJ. Additionally, a fine-grained zone forms at the boundary of the SZ, which strengthens the bonding between materials in the SZ and its boundary, thereby enhancing the load-bearing capacity inside WJ. Secondly, the fracture location coincides with the LMZ within the HAZ. The excessive heat input intensifies the softening effect in this zone, reducing its load-bearing capacity. Thirdly, previous studies have indicated that the outer region of the SZ was positioned in the zone where residual tensile and compressive stresses converge [70]. This abrupt stress variation increases the susceptibility of this zone to failure. The combined influence of these factors leads to the initiation of the original crack outside the SZ.

4. Discussion

Similar to the behavior observed in RFSSW of 6061 and 7075 aluminum alloys, the plunge depth also has a significant effect on the performance of Cu-Cu joints [28-31]. As shown in Fig. 11, the T-SFL of the WJs reaches its maximum when the plunge depth is 1.4 mm, while both insufficient and excessive plunge depths lead to reduced joint strength. The enhanced joint strength at a plunge depth of 1.4 mm is primarily attributed to the improved bonding quality within the SZ and the relatively mitigated softening effect in the HAZ. At this depth, the welding tool penetrates sufficiently into the bottom plate, promoting adequate plastic deformation and material mixing within the SZ, thereby strengthening the metallurgical bonding. In addition, the fine-grained structure formed at the SZ boundary also helps to suppress the initiation and propagation of cracks in this zone. Although the HAZ tends to soften under heat input and can easily become a strength weakness of the WJ, the welding temperature at 1.4 mm plunge depth is lower than that at 1.6 mm. As a result, the associated heat input is reduced, leading to a weaker softening effect and contributing to an increase in load-bearing capacity. For Cu welds, the strength of the WJ is largely constrained by the softening effect in the HAZ. How to regulate heat input to minimize the negative effects of the HAZ while ensuring that the material in the SZ is adequately stirred, mixed, and bonded is a critical topic for further research.

5. Conclusions

This study focuses on the effect of plunge depth on the microstructure and mechanical properties of Cu-Cu joints fabricated by RFSSW. The key findings are outlined below:

(1) As the plunge depth increases, the welding time is prolonged, leading to greater heat input and more pronounced microstructural coarsening. Excessive plunge depth leads to severe softening of the material in the HAZ outside the SZ.

(2) The T-SFL of the WJ first rises and subsequently declines as the plunge depth increases, with the optimal plunge depth found to be 1.4 times the plate thickness. When the plunge depth is less than the thickness of the top plate, the weak areas of the WJs are located at the boundary of the SSZ. However, when the plunge depth exceeds the top plate thickness, failure occurs in the HAZ outside the SZ.

(3) It is feasible to fabricate Cu-Cu joints by RFSSW, and sound welding quality can be achieved under appropriate process parameters. Material softening induced by excessive heat input is a critical factor that limits the load-bearing capacity of the joints and represents a key issue to be addressed in future studies on Cu-Cu welding.

Acknowledgments

The authors gratefully acknowledge the financial support from the National Natural Science Foundation of China (No. 52405479), the Key Research Project of Natural Science in Anhui Higher Education Institutions (No. 2022AH051947), the Anhui Province Excellent Young Teacher Cultivation Project (No. YQYB2024066 and No. YQYB2024065), the Open Research Project of Anhui Simulation Design and Modern Manufacture Engineering Technology Research Center (No. SGCZXYB2302), and the Research Project of Huangshan University (No. HSXYSSD006).

REFERENCES

[1] D. Ólafsson, P. Vilaça, J. Vesanko, Multiphysical characterization of FSW of aluminum electrical busbars with copper ends. Weld. World **64** (1), 59-71 (2020).
DOI: https://doi.org/10.1007/s40194-019-00814-0

[2] A. Forsström, S. Bossuyt, Y. Yagodzinskyy, K. Tsuzaki, H. Hänninen, Strain localization in copper canister FSW welds for spent nuclear fuel disposal. J. Nucl. Mater. **523**, 347-359 (2019).
DOI: https://doi.org/10.1016/j.jnucmat.2019.06.024

[3] A. Heidarzadeh, M. Jabbari, M. Esmaily, Prediction of grain size and mechanical properties in friction stir welded pure copper joints using a thermal model. Int. J. Adv. Manuf. Tech. **77** (9), 1819-1829 (2015).
DOI: https://doi.org/10.1007/s00170-014-6543-7

[4] A. Das, D. Li, D. Williams, D. Greenwood, Joining technologies for automotive battery systems manufacturing. World Electr. Veh. J. **9** (2), 22 (2018).
DOI: https://doi.org/10.3390/wevj9020022

[5] G. Li, L. Zhou, W. Zhou, X. Song, Y. Huang, Influence of dwell time on microstructure evolution and mechanical properties of dissimilar friction stir spot welded aluminum-copper metals. J. Mater. Res. Technol. **8** (3), 2613-2624 (2019).
DOI: https://doi.org/10.1016/j.jmrt.2019.02.015

[6] X.W. Yang, T. Fu, W.Y. Li, Friction stir spot welding: A review on joint macro- and microstructure, property, and process modelling. Adv. Mater. Sci. Eng. **2014** (1), 697170 (2014).
DOI: https://doi.org/10.1155/2014/697170

[7] N. Kumar, I. Masters, A. Das, In-depth evaluation of laser-welded similar and dissimilar material tab-to-busbar electrical interconnects for electric vehicle battery pack. J. Manuf. Processes **70**, 78-96 (2021). DOI: https://doi.org/10.1016/j.jmapro.2021.08.025

[8] A. Das, R. Fritz, M. Finuf, I. Masters, Blue laser welding of multi-layered AISI 316L stainless steel micro-foils. Opt. Laser Technol. **132**, 106498 (2020). DOI: https://doi.org/10.1016/j.optlastec.2020.106498

[9] R. Beygi, R.J.C. Carbas, E.A.S. Marques, A.Q. Barbosa, M.M. Kasaei, L.F.M. da Silva, Mechanism of toughness enhancement of brittle fracture by intermittent η-intermetallic in Al/Cu joint made by FSW. Mat. Sci. Eng. A **890**, 145907 (2024). DOI: https://doi.org/10.1016/j.msea.2023.145907

[10] J.J. Shen, H.J. Liu, F. Cui, Effect of welding speed on microstructure and mechanical properties of friction stir welded copper. Mater. Des. **31** (8), 3937-3942 (2010). DOI: https://doi.org/10.1016/j.matdes.2010.03.027

[11] P. Xue, G.M. Xie, B.L. Xiao, Z.Y. Ma, L. Geng, Effect of heat input conditions on microstructure and mechanical properties of friction-stir-welded pure copper. Metall. Mater. Trans. A **41** (8), 2010-2021 (2010). DOI: https://doi.org/10.1007/s11661-010-0254-y

[12] J.P. Davim, Welding technology, Springer, 2021.

[13] Y.F. Sun, H. Fujii, Investigation of the welding parameter dependent microstructure and mechanical properties of friction stir welded pure copper. Mat. Sci. Eng. A **527** (26), 6879-6886 (2010). DOI: https://doi.org/10.1016/j.msea.2010.07.030

[14] R.S. Mishra, Z.Y. Ma, Friction stir welding and processing. Mater. Sci. Eng. R Rep. **50** (1), 1-78 (2005). DOI: https://doi.org/10.1016/j.mser.2005.07.001

[15] M. Fujimoto, M. Inuzuka, S. Koga, Y. Seta, Development of friction spot joining. Weld. World **49** (3), 18-21 (2005). DOI: https://doi.org/10.1007/BF03266470

[16] Tiwan, M.N. Ilman, Kusmono, Sehono, Microstructure and mechanical performance of dissimilar friction stir spot welded AA2024-O/AA6061-T6 sheets: Effects of tool rotation speed and pin geometry. Int. J. Lightweight Mater. Manuf. **6** (1), 1-14 (2023). DOI: https://doi.org/10.1016/j.ijlmm.2022.07.004

[17] M.S. Mohd Isa, M.R. Muhamad, F. Yusof, N. Yusoff, Z. Brytan, T. Suga, Y. Morisada, H. Fujii, Improved mechanical and electrical properties of copper-aluminum joints with highly aligned graphene reinforcement via friction stir spot welding. J. Mater. Res. Technol. **24**, 9203-9215 (2023). DOI: https://doi.org/10.1016/j.jmrt.2023.05.155

[18] Y. Guishen, C. Xin, W. Zitao, Mechanical performance optimization and microstructure analysis of similar thin AA6061-T6 sheets produced by swept friction stir spot welding. Int. J. Adv. Manuf. Tech. **118** (5), 1829-1841 (2022). DOI: https://doi.org/10.1007/s00170-021-07387-7

[19] S. Suresh, K. Venkatesan, E. Natarajan, S. Rajesh, Performance analysis of nano silicon carbide reinforced swept friction stir spot weld joint in AA6061-T6 alloy, Silicon **13** (10), 3399-3412 (2021). DOI: https://doi.org/10.1007/s12633-020-00751-4

[20] X. Ge, D. Jiang, W. Song, H. Wang, Effects of tool plunging path on the welded joint properties of pinless friction stir spot welding. Lubricants **11** (3), 150 (2023). DOI: https://doi.org/10.3390/lubricants11030150

[21] S. Alaeibehmand, S.E. Mirsalehi, E. Ranjbarnodeh, Pinless FSSW of DP600/Zn/AA6061 dissimilar joints. J. Mater. Res. Technol. **15**, 996-1006 (2021). DOI: https://doi.org/10.1016/j.jmrt.2021.08.071

[22] N. Becker, J.F. dos Santos, B. Klusemann, Experimental investigation of crack propagation mechanism in refill friction stir spot joints of AA6082-T6. Eng. Fract. Mech. **300**, 109963 (2024). DOI: https://doi.org/10.1016/j.engfracmech.2024.109963

[23] A. Derlatka, P. Lacki, Experimental study and numerical simulation of cellular i-beam manufactured using refill friction stir spot welding technology. Thin-Walled Struct. **200**, 111890 (2024). DOI: https://doi.org/10.1016/j.tws.2024.111890

[24] S. Chen, Z. Li, J. Xiao, J. Pu, Y. Han, S. Gai, D. Wang, X. Jiang, Experimental investigation of material flow behavior during refill friction stir spot welding. J. Mater. Process. Technol. **337**, 118710 (2025). DOI: https://doi.org/10.1016/j.jmatprotec.2024.118710

[25] C. Schilling, S.J. dos, Method and device for joining at least two adjoining work pieces by friction welding. USA patent, 6722556, 2004.

[26] D. Zhang, J. Dong, J. Xiong, N. Jiang, J. Li, W. Guo, Microstructure characteristics and corrosion behavior of refill friction stir spot welded 7050 aluminum alloy. J. Mater. Res. Technol. **20**, 1302-1314 (2022). DOI: https://doi.org/10.1016/j.jmrt.2022.07.152

[27] Y. Zou, W. Li, X. Yang, Y. Su, Q. Chu, Z. Shen, Microstructure and mechanical properties of refill friction stir spot welded joints: Effects of tool size and welding parameters. J. Mater. Res. Technol. **21**, 5066-5080 (2022). DOI: https://doi.org/10.1016/j.jmrt.2022.11.108

[28] V.S. Janga, M. Awang, Influence of plunge depth on temperatures and material flow behavior in refill friction stir spot welding of thin AA7075-T6 sheets: A numerical study. Metals **12** (6), 927 (2022). DOI: https://doi.org/10.3390/met12060927

[29] A. Kubit, K. Faes, H. Aghajani Derazkola, Refill friction stir spot welding tool plunge depth effects on shear, peel, and fatigue properties of alclad coated AA7075 aluminum joints. Int. J. Fatigue **185**, 108308 (2024). DOI: https://doi.org/10.1016/j.ijfatigue.2024.108308

[30] L. Zhou, L.Y. Luo, R. Wang, J.B. Zhang, Y.X. Huang, X.G. Song, Process parameter optimization in refill friction spot welding of 6061 aluminum alloys using response surface methodology. J. Mater. Eng. Perform. **27** (8), 4050-4058 (2018). DOI: https://doi.org/10.1007/s11665-018-3472-x

[31] D.C. Bîrsan, V. Păunoiu, V.G. Teodor, Neural networks applied for predictive parameters analysis of the refill friction stir spot welding process of 6061-T6 aluminum alloy plates. Materials **16** (13), 4519 (2023). DOI: https://doi.org/10.3390/ma16134519

[32] G. Sun, L. Zhou, R. Zhang, L. Luo, H. Xu, H. Zhao, N. Guo, D. Zhang, Effect of sleeve plunge depth on interface/mechanical characteristics in refill friction stir spot welded joint. Acta Metall. Sin. (Engl. Lett.) **33** (4), 551-560 (2020). DOI: https://doi.org/10.1007/s40195-019-00968-2

[33] Y. Yue, Y. Shi, S. Ji, Y. Wang, Z. Li, Effect of sleeve plunge depth on microstructure and mechanical properties of refill friction stir spot welding of 2198 aluminum alloy. J. Mater. Eng. Perform. **26** (10), 5064-5071 (2017).
DOI: https://doi.org/10.1007/s11665-017-2929-7

[34] Y.Q. Zhao, H.J. Liu, S.X. Chen, Z. Lin, J.C. Hou, Effects of sleeve plunge depth on microstructures and mechanical properties of friction spot welded alclad 7B04-T74 aluminum alloy. Mater. Des. **62**, 40-46 (2014).
DOI: https://doi.org/10.1016/j.matdes.2014.05.012

[35] Y. Wang, P. Chai, Characteristics and tensile-shear properties of refill FSSW joint under different plunge depths in 2060 aluminum alloy. Arch. Metall. Mater. **66**, 451-460 (2021).
DOI: https://doi.org/10.24425/amm.2021.135878

[36] Y. Zou, W. Li, Q. Chu, Z. Shen, F. Wang, H. Tang, A. Vairis, L. Liu, The impact of macro/microstructure features on the mechanical properties of refill friction stir spot–welded joints of AA2219 alloy with a large thickness ratio. Int. J. Adv. Manuf. Tech. **112** (11), 3093-3103 (2021).
DOI: https://doi.org/10.1007/s00170-020-06504-2

[37] Y. Yuan, Z. Wu, K. Chen, H. Liu, H. Huang, Y. Li, Effects of plunge depth on macro-/microstructure and mechanical properties of refill friction stir spot welded 2195-T6 Al-Li alloy. J. Mater. Res. Technol. **35**, 6026-6041 (2025).
DOI: https://doi.org/10.1016/j.jmrt.2025.02.046

[38] B.H. Silva, G. Zepon, C. Bolfarini, J.F. dos Santos, Refill friction stir spot welding of AA6082-T6 alloy: Hook defect formation and its influence on the mechanical properties and fracture behavior. Mat. Sci. Eng. A **773**, 138724 (2020).
DOI: https://doi.org/10.1016/j.msea.2019.138724

[39] P. Maruschak, I. Konovalenko, A. Sorochak, Methods for evaluating fracture patterns of polycrystalline materials based on the parameter analysis of ductile separation dimples: A review. Eng. Fail. Anal. **153**, 107587 (2023).
DOI: https://doi.org/10.1016/j.engfailanal.2023.107587

[40] Y. Li, G. Sun, Z. Zhang, L. Zhou, N. Guo, Q. Meng, J. Dong, H. Zhao, Texture evolution of refill friction stir spot welding in alclad 2A12-T42 aluminum alloy. Mater. Charact. **205**, 113289 (2023). DOI: https://doi.org/10.1016/j.matchar.2023.113289

[41] D. Gera, B. Fu, U.F.H.R. Suhuddin, A. Plaine, N. Alcantara, J.F. dos Santos, B. Klusemann, Microstructure, mechanical and functional properties of refill friction stir spot welds on multilayered aluminum foils for battery application. J. Mater. Res. Technol. **13**, 2272-2286 (2021).
DOI: https://doi.org/10.1016/j.jmrt.2021.06.017

[42] J. Draper, S. Fritsche, S. de Traglia Amancio-Filho, A. Galloway, A. Toumpis, Exploring a novel chamfered tool design for short duration refill friction stir spot welds of high strength aluminium. Int. J. Adv. Manuf. Tech. **131** (12), 5867-5879 (2024).
DOI: https://doi.org/10.1007/s00170-024-13336-x

[43] Z. Liu, Z. Fan, L. Liu, S. Miao, Z. Lin, C. Wang, Y. Zhao, R. Xin, C. Dong, Refill friction stir spot welding of az31 magnesium alloy sheets: Metallurgical features, microstructure, texture and mechanical properties. J. Mater. Res. Technol. **23**, 3337-3350 (2023). DOI: https://doi.org/10.1016/j.jmrt.2023.01.151

[44] W.C. Ke, J.P. Oliveira, S.S. Ao, F.B. Teshome, L. Chen, B. Peng, Z. Zeng, Thermal process and material flow during dissimilar double-sided friction stir spot welding of AZ31/ZK60 magnesium alloys. J. Mater. Res. Technol. **17**, 1942-1954 (2022).
DOI: https://doi.org/10.1016/j.jmrt.2022.01.097

[45] H.f. Zhang, L. Zhou, W.l. Li, G.h. Li, Y.t. Tang, N. Guo, J.c. Feng, Effect of tool plunge depth on the microstructure and fracture behavior of refill friction stir spot welded AZ91 magnesium alloy joints. Int. J. Miner. Metall. Mater. **28** (4), 699-709 (2021).
DOI: https://doi.org/10.1007/s12613-020-2044-x

[46] D. Kim, S. Baek, M. Nishijima, H.c. Lee, P. Geng, N. Ma, Z. Zhang, H. Park, C. Chen, S.J. Lee, K. Suganuma, Toward defect-less and minimized work-hardening loss implementation of al alloy/high-purity Cu dissimilar lap joints by refill friction stir spot welding for battery tab-to-busbar applications. Mat. Sci. Eng. A **892**, 146089 (2024).
DOI: https://doi.org/10.1016/j.msea.2024.146089

[47] Y. Zuo, L. Kong, Z. Liu, Z. Lv, H. Wen, Process parameters optimization of refill friction stir spot welded Al/Cu joint by response surface method. Trans. Indian Inst. Met. **73** (12), 2975-2984 (2020).
DOI: https://doi.org/10.1007/s12666-020-02100-w

[48] Z. Shen, Y. Ding, W. Guo, W. Hou, X. Liu, H. Chen, F. Liu, W. Li, A. Gerlich, Refill friction stir spot welding al alloy to copper via pure metallurgical joining mechanism. Chin. J. Mech. Eng. **34** (1), 75 (2021).
DOI: https://doi.org/10.1186/s10033-021-00593-0

[49] Friction stir spot welding-aluminium and aluminium alloys: Part 5: Quality and inspection requirements, GB/T 41979.5-2022, National Standard of the People's Republic of China, Standards Press of China, 2022.

[50] S. Ji, Y. Wang, J. Zhang, Z. Li, Influence of rotating speed on microstructure and peel strength of friction spot welded 2024-T4 aluminum alloy. Int. J. Adv. Manuf. Tech. **90** (1), 717-723 (2017).
DOI: https://doi.org/10.1007/s00170-016-9398-2

[51] S. Ji, Z. Li, Y. Wang, L. Ma, L. Zhang, Material flow behavior of refill friction stir spot welded LY12 aluminum alloy. High Temp. Mater. Process. **36** (5), 495-504 (2017).
DOI: https://doi.org/10.1515/htmp-2015-0254

[52] H.F. Zhang, L. Zhou, G.H. Li, Y.T. Tang, W.L. Li, R. Wang, Prediction and validation of temperature distribution and material flow during refill friction stir spot welding of AZ91D magnesium alloy. Sci. Technol. Weld. Joining **26** (2), 153-160 (2021).
DOI: https://doi.org/10.1080/13621718.2020.1864864

[53] S. Fritsche, F. Schindler, W.S. de Carvalho, S.T. Amancio-Filho, Wear mechanisms and failure analysis of a tool used in refill friction stir spot welding of AA6061-T6. Wear **560-561**, 205610 (2025). DOI: https://doi.org/10.1016/j.wear.2024.205610

[54] G. Zhou, T. Huang, L. Su, Q. Huang, S. Wu, B. Zhang, The microstructure and mechanical properties of deposited alcusc alloy wall structures fabricated by waam with FSP assistance. Thin-Walled Struct. **209**, 112954 (2025).
DOI: https://doi.org/10.1016/j.tws.2025.112954

[55] E. Berger, M. Miles, A. Curtis, P. Blackhurst, Y. Hovanski, 2D axisymmetric modeling of refill friction stir spot welding and ex-

perimental validation. J. Manuf. Mater. Process. **6** (4), 89 (2022). DOI: https://doi.org/10.3390/jmmp6040089

[56] Y. Zhao, H. Liu, T. Yang, Z. Lin, Y. Hu, Study of temperature and material flow during friction spot welding of 7B04-T74 aluminum alloy. Int. J. Adv. Manuf. Tech. **83** (9), 1467-1475 (2016). DOI: https://doi.org/10.1007/s00170-015-7681-2

[57] J. Xiong, X. Peng, J. Shi, Y. Wang, J. Sun, X. Liu, J. Li, Numerical simulation of thermal cycle and void closing during friction stir spot welding of AA-2524 at different rotational speeds. Mater. Charact. **174**, 110984 (2021). DOI: https://doi.org/10.1016/j.matchar.2021.110984

[58] W.H. Liu, Y. Wu, J.Y. He, T.G. Nieh, Z.P. Lu, Grain growth and the Hall-petch relationship in a high-entropy fecrnicomn alloy. Scr. Mater. **68** (7), 526-529 (2013). DOI: https://doi.org/10.1016/j.scriptamat.2012.12.002

[59] Q. Sun, H.-S. Di, J.-C. Li, B.-Q. Wu, R.D.K. Misra, A comparative study of the microstructure and properties of 800Mpa microalloyed C-Mn steel welded joints by laser and gas metal arc welding. Mat. Sci. Eng. A **669**, 150-158 (2016). DOI: https://doi.org/10.1016/j.msea.2016.05.079

[60] I.C. Choi, Y.J. Kim, Y.M. Wang, U. Ramamurty, J.i. Jang, Nanoindentation behavior of nanotwinned Cu: Influence of indenter angle on hardness, strain rate sensitivity and activation volume. Acta Mater. **61** (19), 7313-7323 (2013). DOI: https://doi.org/10.1016/j.actamat.2013.08.037

[61] P. Chai, W. Hu, S. Ji, X. Ai, Z. Lv, Q. Song, Refill friction stir spot welding dissimilar Al/Mg alloys. J. Mater. Eng. Perform. **28** (10), 6174-6181 (2019). DOI: https://doi.org/10.1007/s11665-019-04359-7

[62] Z. Dong, Q. Song, X. Ai, Z. Lv, Effect of joining time on intermetallic compound thickness and mechanical properties of refill friction stir spot welded dissimilar Al/Mg alloys. J. Manuf. Process. **42**, 106-112 (2019). DOI: https://doi.org/10.1016/j.jmapro.2019.04.013

[63] Y. Zou, W. Li, Q. Chu, D. Wu, Y. Su, Z. Shen, F. Wang, H. Tang, Formability and mechanical property of refill friction stir spot-welded joints. Weld. World **65** (5), 899-907 (2021). DOI: https://doi.org/10.1007/s40194-020-01056-1

[64] G. Yu, X. Chen, Z. Wu, Y. Chen, G. Zhang, Analysis of microstructure and mechanical properties of probeless friction stir spot welding joint in AA6061-T6 aluminum thin plate. J. Jilin Univ. (Eng. Technol. Ed.) **53** (5), 1338-1344 (2023). DOI: https://doi.org/10.13229/j.cnki.jdxbgxb.20210937

[65] L.C. Campanelli, U.F.H. Suhuddin, A.Í.S. Antonialli, J.F. dos Santos, N.G. de Alcântara, C. Bolfarini, Metallurgy and mechanical performance of AZ31 magnesium alloy friction spot welds. J. Mater. Process. Technol. **213** (4), 515-521 (2013). DOI: https://doi.org/10.1016/j.jmatprotec.2012.11.002

[66] E. Gadalińska, A. Kubit, T. Trzepieciński, G. Moneta, Experimental and numerical stress state assesment in refill friction stir spot welding joints. Fatigue Aircr. Struct. **2021** (13), 54-71 (2021). DOI: https://doi.org/doi:10.2478/fas-2021-0006

[67] T. Rosendo, M. Tier, J. Mazzaferro, C. Mazzaferro, T.R. Strohaecker, J.F. Dos Santos, Mechanical performance of AA6181 refill friction spot welds under lap shear tensile loading. Fatigue Fract. Eng. M. **38** (12), 1443-1455 (2015). DOI: https://doi.org/10.1111/ffe.12312

[68] X. Wang, J. Ahn, C. Kaboglu, L. Yu, B.R.K. Blackman, Characterisation of composite-titanium alloy hybrid joints using digital image correlation. Compos. Struct. **140**, 702-711 (2016). DOI: https://doi.org/10.1016/j.compstruct.2015.12.023

[69] A.H. Plaine, U.F.H. Suhuddin, N.G. Alcântara, J.F. dos Santos, Microstructure and mechanical behavior of friction spot welded AA6181-T4/Ti6al4v dissimilar joints. Int. J. Adv. Manuf. Tech. **92** (9), 3703-3714 (2017). DOI: https://doi.org/10.1007/s00170-017-0439-2

[70] X. Ge, I.N. Kolupaev, D. Jiang, W. Song, H. Wang, Influence of rotational speed on the microstructure and mechanical properties of refill friction stir spot welded pure copper. Crystals **15** (3), 268 (2025). DOI: https://doi.org/10.3390/cryst15030268